



UNIVERSIDAD NACIONAL AUTÓNOMA DE MÉXICO

FACULTAD DE INGENIERÍA

**Accurate Design,
Simulation and
Implementation of AC/DC
Inductors for Power
Electronic Converters**

ARTÍCULO ACADÉMICO

Que para obtener el título de
Ingeniero Eléctrico – Electrónico

P R E S E N T A

Elean Jim Martínez Salgado


ASESOR DE ARTÍCULO ACADÉMICO

Dr. Mario Roberto Arrieta Paternina



Ciudad Universitaria, Cd. Mx., 2024

Accurate design, simulation and implementation of AC/DC inductors for power electronic converters

Elean Jim Martínez-Salgado¹ | Gabriel E. Mejía-Ruiz² | José Manuel Ramos-Guerrero¹ |
Mario R. Arrieta Paternina¹  | Javier de la Cruz³ | Harold R. Chamorro⁴ 

¹National Autonomous University of Mexico (UNAM, in Spanish), Mexico City, Mexico

²University of Central Florida (UCF), Orlando, Florida, USA

³CONAHCYT-ITSON, Mexico City, Sonora, Mexico

⁴KTH Royal Institute of Technology, Stockholm, Sweden

Correspondence

Harold R. Chamorro, KTH, Royal Institute of Technology, Stockholm, Sweden.
Email: hrcv@kth.se

Funding information

Dirección General de Asuntos del Personal Académico, Universidad Nacional Autónoma de México, Grant/Award Number: IT102723

Abstract

This article proposes a holistic and improved methodology for the inductors' design in power electronic circuits operating at high frequencies. This methodology includes an analytical design, a finite element modeling of the electromagnetic behavior with JMAG software, a simulation analysis in a Simulink environment, and experimental verification of the effectiveness of inductor design in a laboratory-scale step-up boost power converter prototype. The holistic approach allowed us to achieve all target specifications such as maximum power (300 W), minimum voltage (60 V), inductance (1.77 mH), and maximum current ripple (1 A). It guarantees the losses' minimization in core and copper (21.47 W), and marginal errors below 4% between the analytical, simulated, and experimental values.

1 | INTRODUCTION

Power electronic converters are indispensable to achieve the energy conversion process in many applications such as full cells, battery energy storage systems, electric chargers, electric vehicles, solar generation, DC loads etc. [1–3]. In particular, DC-DC power converters are used in such applications to step up/down the DC voltage [1, 4], where magnetic inductors play a key role in regulating the output voltage since they smooth out the pulses thanks to their capability in storing and releasing energy and filter to generate stable output with the output capacitor. In this context, the topology of the step-up DC-DC boost converter in Figure 1 utilizes one high-frequency power device operating at a high switching frequency with minimum switching losses. After defining topology and power device, the inductor's design makes up a degree of freedom to optimize its performance [5].

1.1 | Literature review

According to the literature, conventional inductor design strategies are established according to their application such as filtering that is used in high-frequency power converters and pulse-width-modulators switched regulators, and regulation in AC system, existing two typical methods for designing based on the area product A_p or the geometric constant K_g [6–8]. The area-product approach is widely used to design inductors, especially when they undergo pulse width modulations (PWM) in DC-DC power electronic converters. It associates the geometrical core parameters with the magnetic and electric parameters. Meanwhile, the K_g approach uses the core geometry, allowing the estimation of core geometry for specific targets [9]. It does not consider the current density of the conductor, thus if the maximum current density is exceeded, a new iteration is executed until this criterion is fulfilled [10]. Both methodologies use

This is an open access article under the terms of the [Creative Commons Attribution](https://creativecommons.org/licenses/by/4.0/) License, which permits use, distribution and reproduction in any medium, provided the original work is properly cited.

© 2024 The Author(s). *IET Power Electronics* published by John Wiley & Sons Ltd on behalf of The Institution of Engineering and Technology.

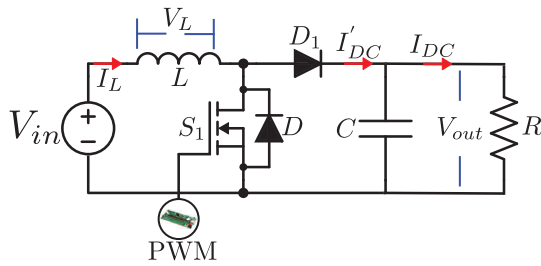


FIGURE 1 Diagram of the typical step-up DC-DC electronic converter.

target definitions for designing such as the maximum flux density (\mathbf{B}_{max}) or maximum current density (\mathbf{J}_{max}), implying many iterations to meet the design requirements.

On the other hand, other approaches focus on minimizing the core and copper losses which are optimized together with the current ripple for the inductor design [5, 11–13]. Also, approaches based on artificial neural networks have been exploited considering physics-informed features for the modeling and optimization of inductor's design [14].

1.2 | Problem statement

Nowadays, inductor design methodologies for power electronic circuits provide guidelines for using a basic set of fundamental rules [6]. However, the switching frequency in electronic converters is gradually increasing, aiming to increase the power density of the system [10]. In the design process, the selection of magnetic components for the core, the types of conductors, and the treatment of non-sinusoidal excitation waveforms are design constraints that must be carefully considered [13].

Additionally, the reduction of power losses in the coils used in power electronic converters is becoming increasingly relevant due to the reduction of conduction and switching losses in wide bandgap semiconductors [5]. Reported strategies are often based on several assumptions going back more than two decades [8, 10, 15], many of these assumptions are only valid in a context of frequencies greater than 1 MHz, and for low power converters (>100 W) [13]. Consequently, direct use of these procedures for medium- and high-power applications may require a significant number of design iterations and may even result in unbuildable or underperforming designs.

1.3 | Contribution

To counteract the abovementioned problems, this investigation proposes a holistic and improved methodology for the inductors' design in power electronic circuits operating in the intermediate frequency range (between 5 KHz and 100 kHz). The design methodology proposes design equations, a simple finite element simulation of the electromagnetic behavior with JMAG software, and experimental verification of the effectiveness of inductor design in a laboratory-scale boost power converter prototype.

The major contributions of this investigation lie in:

- A simple and reliable methodology to accurately design, analyze, and implement inductors for their integration in power electronic converters given their proliferation due to the penetration growth of renewable energy sources. This methodology is supported by the finite element method and powered by Maxwell's equations that facilitate the computation of the magnetic flux density throughout the core and provide a precise behavior of the coil in time.
- The finite element method is a key contribution to the design methodology. It represents the interface between the basic sizing equations and the fabrication of the prototype. The simulation by FEM considers accurately all non-linearities of the material's magnetic properties. Copper and core losses and waveform quality can be predicted and corrected precisely before manufacturing.
- The accuracy and reliability of the proposed inductor design process are rigorously validated through experiments with a laboratory prototype. Measurements carried out on the laboratory prototype show a remarkable alignment between theoretical deductions, simulation results, and real-world performance. In particular, the discrepancies between the measured data and the theoretically calculated values present an error margin of less than 4%, underlining the robustness and accuracy of the proposed design methodology. This validation process ensures the confidence and feasibility of the straightforward design method proposed for inductor design in practical power electronics applications.

1.4 | Organization

The rest of the paper is organized as follows. The mathematical foundations of the inductor's design are described in Section 2 with a holistic design methodology. The application in power electronics is described in Section 3. The performance of the electromagnetic design is explained in Section 4, where geometry, materials, and operational conditions are introduced. The behavior of the DC-DC converter in simulation and prototype is explained in Section 5. Finally, conclusions have been made in Section 7.

2 | INDUCTOR HOLISTIC DESIGN

In this section, we adopt a holistic strategy to design a DC inductor for power electronic converters, for instance, the step-up DC-DC boost converter in Figure 1. This strategy allows us to adapt to the inductor's requirements, such as maximum power (P_{max}), minimum voltage (V_{min}), maximum current ripple (δI_{max}), inductance (L), coil sizing, and number of turns (n) that directly affect the wire resistance (R_{Cu}). Besides the target definitions, this methodology requires as input parameters the physical and magnetic features of a commercial core and the electrical and physical characteristics of the wire, as summarized in Table 1.

TABLE 1 Target definitions and physical, magnetic and electrical characteristics.

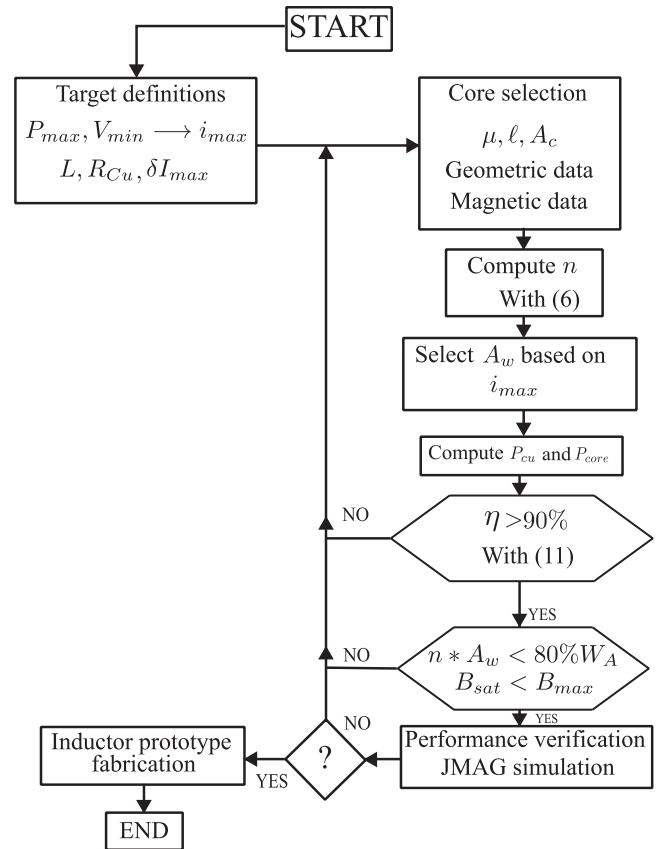
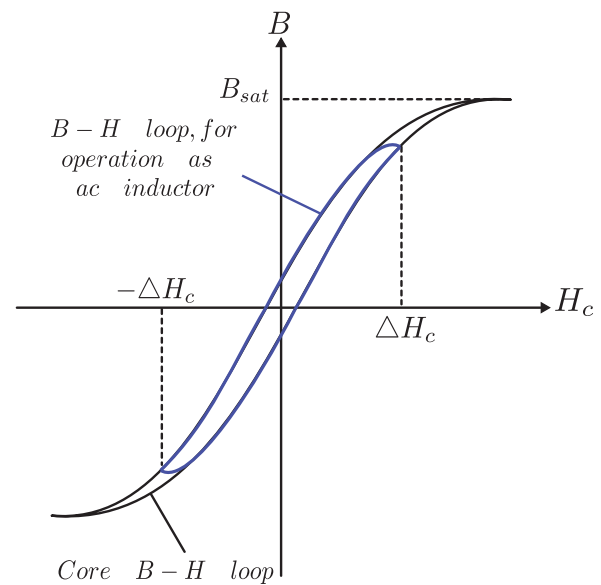
Parameter	Value
Inputs	
Maximum power (P_{max}), minimum voltage (V_{min})	300 W, 60 V
Inductance (L), maximum flux density (B_{MAX})	1.77 mH, 1.44 T
Magnetic permeability (μ), magnetic length (ℓ)	40, 131.4 mm
Cross-sectional area of the core (A_c), mean length per turn (MLT)	600 mm ² , 138.6 mm
Saturation flux density (B_{SAT})	1.6 T
Maximum current (i_{max}), maximum current ripple (δI_{MAX})	5.4 A, 1 A
Cross-sectional area of the wire (A_w)	2.08 mm ²
Efficiency (η), wire length (l_{Cu})	92.8%, 1.4 m
Wire resistance (R_{Cu})	0.4 Ω
Outputs	
Core losses (P_{core})	12.9 W
Number of turns (n)	104 turns
Wire losses in copper (P_{Cu})	8.57 W

The inductor is designed by implementing an iterative process to comply with a set of operational conditions. In this work, the inductor is designed by the utilization of a commercial general-purpose magnetic core which is massively produced. Meanwhile, the coil is designed to conform to the operational conditions of the inductor based on the core's geometry and its magnetic properties. The flowchart of the inductor design is showcased in Figure 2. It starts defining targets according to the step-up DC-DC boost converter in Figure 1, such as the maximum power (P_{max}), the minimum voltage (V_{min}), and the peak current (i_{max}) that flows through the inductor. Likewise, the manufacturer information specified in the core datasheet together with the AWG caliber and the number of turns (n), the cross-sectional area of the wire (A_w), and their associated losses with the copper (P_{Cu}) and core due to the hysteresis phenomenon yielded by the magnetic field (H_c) variations, as depicted in Figure 3. After all previous computations meet the target definitions in Figure 2, JMAG[®] is used to model and obtain the coil inductance via the finite element method with the parameter in Table 1.

In this investigation, target definitions are oriented to the inductor applications in power electronic converters. Since we deal with a step-up DC-DC converter, then we seek to maximize the power and minimize the coil size and the current ripple together with losses. For instance, the current ripple is expected around 1A.

2.1 | Preliminary analytical design

The electromagnetic fundamentals derived from Faraday's and Ampere's laws are utilized in this section to establish the main relationships between electromotive force and the concatenated

**FIGURE 2** Holistic design methodology for the inductor.**FIGURE 3** Hysteresis loop for operation as AC inductor.

magnetic flux (ϕ) flowing through the magnetic circuit (ℓ); the magnetic flux is assumed constant all along the transversal area (A_c) of the core due to its isotropic characteristics. These two principles allow us to establish the relationship between the inductor voltage and the magnetic flux density, where the

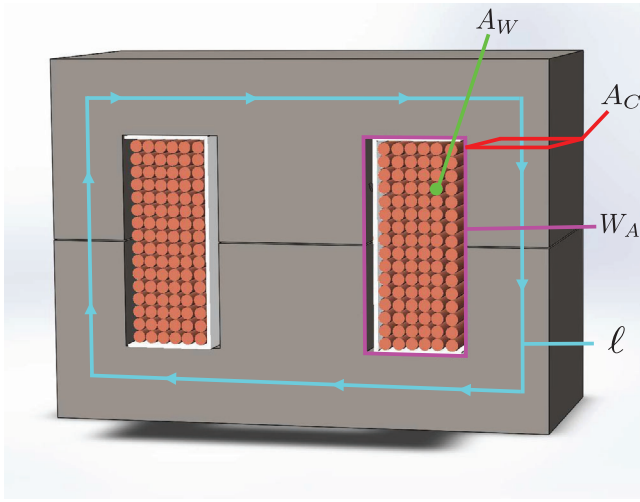


FIGURE 4 Main physical sections of the inductor.

induced voltage is proportional to the number of turns (n), the area of the transversal section of the core (A_c) and the magnetic flux density (\mathbf{B}), and the cross-sectional area of the wire A_w that limits the inductor power. Likewise, the area of the core window (W_A) that in turn limits the number of turns and the wire gauge to be used. Geometric variables such as A_C , A_w , W_A , and ℓ are shown in Figure 4. Thus, the voltage becomes

$$v(t) = n \frac{d(\mathbf{B}A_C)}{dt}. \quad (1)$$

It is noteworthy to remark that (1) establishes the relationship between the physical parameters of the coil and the induced voltage. Likewise, Ampere's law together with the constitutive relation $\mathbf{B} = \mu\mathbf{H}$ enables to, respectively, re-write (1) in terms of the magnetic field intensity (\mathbf{H}) and the coil current ($i(t)$), as follows:

$$v(t) = \mu n A_C \frac{dH}{dt}, \quad (2)$$

$$v(t) = \frac{\mu n^2 A_C}{\ell} \frac{di}{dt}. \quad (3)$$

Due to the inductor voltage is defined by $v(t) = L di/dt$, then the inductance of the coil can be expressed as:

$$L = \frac{\mu n^2 A_C}{\ell}. \quad (4)$$

Since L is a target definition parameter, then the number of turns becomes

$$n = \sqrt{\frac{L\ell}{\mu A_C}}, \quad (5)$$

where ℓ stands for the magnetic length and depends on the core dimensions. The parameter for the number of turns allows to

obtain the length of the wire that is defined by:

$$l_{Cu} = n(MLT), \quad (6)$$

where MLT represents the mean length per turn.

By using the Ampere's law and the constitutive relationship $\mathbf{B} = \mu\mathbf{H}$, the coil current is given by

$$i(t) = \frac{\mathbf{H}\ell}{n} = \frac{\mathbf{B}\ell}{\mu n}. \quad (7)$$

Then, the saturation current is determined in function of the \mathbf{B}_{sat} , such that

$$i_{sat} = \frac{\mathbf{B}_{sat}\ell}{\mu n}. \quad (8)$$

The losses associated with the Joule effect are given by

$$P_{Cu} = I_{RMS}^2 R_{Cu}, \quad (9)$$

where I is the RMS inductor current and $R_{Cu} = \rho l_{Cu}/A_w$, ρ stands for the electrical resistivity, l_{Cu} represents the length of the conductor, and A_w symbolizes the transversal area of the conductor. Since the inductor current is a target to be met in the holistic methodology depicted in Figure 2, A_w can be chosen according to the American wire gauge (AWG) calibers. Thus, the selected wire is No. AWG 14, since it complies with the criterion of the window area and the maximum current capacity computed in Table 1.

To compute the core losses, JMAG employs the frequency separation method assuming that hysteresis losses are proportional to the frequency and Eddy current losses are associated with the square of the frequency [16]. Thus, the losses P_{core} for a known magnetic flux density are given by:

$$P_{core} = a(\mathbf{B}) \times f + b(\mathbf{B}, f) \times f^2, \quad (10)$$

where $a(\mathbf{B})$ represents the hysteresis losses and $b(\mathbf{B}, f)$ stands for the Eddy current losses. The efficiency (η) in (11) is also established as a target to be met, and it must be above 90%.

$$\eta = \left(1 - \frac{P_{Cu} + P_{core}}{P_{max}}\right) * 100\%. \quad (11)$$

Another target definition is related to the total areas that will cover the copper (nA_w) and the core window (W_A). To this end, the target to be met is subjected to $nA_w < 0.8W_A$. However, if linear changes are assumed in $i(t) = \mathbf{B}l/\mu n$, then the number of turns becomes $n = \Delta i l / \Delta \mathbf{B} A_c$, resulting in:

$$\frac{\Delta i l}{\Delta \mathbf{B} A_c} A_w < 0.8 W_A, \quad (12)$$

where (12) describes the relationships between the conductor current (i), the magnetic flux density (\mathbf{B}), the transversal area (A_c), the wished inductance (L), and the total area utilized by the conductor (A_w). In the worst condition, the ripple current and the flux density, respectively, achieve $\Delta i = i_{sat}$ and $\Delta \mathbf{B} = \mathbf{B}_{sat}$.

2.2 | Finite element modeling by using JMAG

To effectively model the inductor, this investigation uses JMAG to obtain its electromagnetic performance and to derive its electrical parameters. The inductor model conceives the differential form of Maxwell's equations in (13) and their constitutive relations given by $\mathbf{D} = \epsilon\mathbf{E}$, $\mathbf{B} = \mu\mathbf{H}$, and $\mathbf{J} = \sigma\mathbf{E}$, where μ , ϵ and σ symbolize the magnetic permeability, electrical permittivity and electrical conductivity, respectively.

$$\begin{aligned}\nabla \times \mathbf{E} &= -\frac{\partial \mathbf{B}}{\partial t}; & \nabla \cdot \mathbf{D} &= \frac{1}{\sigma}, \\ \nabla \times \mathbf{H} &= \mathbf{J} + \frac{\partial \mathbf{D}}{\partial t}; & \nabla \cdot \mathbf{B} &= 0,\end{aligned}\quad (13)$$

where ∇ , \mathbf{E} , \mathbf{B} , \mathbf{D} , \mathbf{H} , and \mathbf{J} , respectively, stand for the gradient operator, the electric and magnetic fields, the displacement current, the magnetic field intensity, and the electric current density.

The FEM solves the magnetic vector potential (\mathbf{A}) in (14) at every node in a two-dimensional problem formulation, whose curl is expressed in (15). Due to this consideration, this investigation selects a 2D model, which in turn reduces the computations.

$$\mathbf{A} = \mathcal{A}(x, y)\mathbf{k}, \quad (14)$$

where \mathbf{k} is the unit vector in the ξ -direction [17].

$$\mathbf{B} = \nabla \times \mathbf{A}. \quad (15)$$

Given that the displacement current depends on the electromagnetic fields [17]. Then, the inductor design is bounded for high-frequency applications and Ampere's law with Maxwell's addition becomes

$$\nabla \times \mathbf{H} = \mathbf{J} + \frac{\partial \mathbf{D}}{\partial t}. \quad (16)$$

Thus, the coupling between electrical circuits and the magnetic field equations in the inductor is described as:

$$\nabla \times \left(\frac{1}{\mu} \nabla \times \mathbf{A} \right) + \sigma \left(\frac{\partial \mathbf{A}}{\partial t} + \nabla \mathbf{V} \right) - \frac{\partial \mathbf{D}}{\partial t} = 0. \quad (17)$$

Considering small variations of the electric displacement, (17) can be expressed in Cartesian coordinates as

$$\frac{\partial}{\partial x} \left(\frac{\partial \mathcal{A}_\xi}{\partial x} \right) + \frac{\partial}{\partial y} \left(\frac{\partial \mathcal{A}_\xi}{\partial y} \right) \approx \sigma \frac{\partial \mathcal{A}_\xi}{\partial t} + \sigma \nabla \mathbf{V}. \quad (18)$$

Since the inductor's coil is designed using filamentary conductors, the current is uniformly distributed and the electromagnetic operation of the inductor is described by

$$\frac{\partial}{\partial x} \left(\frac{\partial \mathcal{A}_\xi}{\partial x} \right) + \frac{\partial}{\partial y} \left(\frac{\partial \mathcal{A}_\xi}{\partial y} \right) - \frac{1}{\rho} \frac{\partial \mathcal{A}_\xi}{\partial t} + \frac{1}{\rho} \nabla \frac{V_L}{l} \approx 0, \quad (19)$$

where V_L is the voltage applied in the region of finite elements and l is the length of the inductor core (2D geometry). Thereby,

V_L is derived as

$$V_L = R_{Cu} I_L + n l_{Cu} \frac{\partial \mathcal{A}_\xi}{\partial t}, \quad (20)$$

where R_{Cu} symbolizes the DC resistance of the conductor, I_L denotes the total current, and l_{Cu} represents the length of the conductor.

3 | POWER ELECTRONIC APPLICATION

The DC-DC boost is a converter widely studied and referenced by the scientific community. In this work, this circuit is employed to verify the feasibility and coherence of the proposed design method in a real circuit under laboratory conditions [18–21]. The circuit used in this test is composed of an inductor (L), a diode (D_1), a power switch (S_1), and a capacitor (C). The circuit is powered, at its input, with a DC source (V_{in}), and it has a resistive load at its output.

The test circuit is controlled by a pulse width modulation signal (PWM). According to this control signal, two operational states are present in the circuit. The first arises when the PWM signal is in the “ON” state. During this time (t_{on}), the current flows from V_{in} to L , storing energy in the form of an electromagnetic field. The corresponding induced voltage is represented by $V_L(t) = L di_L(t)/dt$. In the period, the second operating state occurs when the PWM is “OFF”, lasting a time of t_{off} . Under these conditions, V_L is added to V_{in} , raising the out voltage (V_{out}). The inductor charging and discharging currents can be depicted by:

$$\blacktriangle i_{L, on} = \frac{1}{L} \int_0^{t_{on}} V_L dt = -\frac{V_{in}}{L} t_{on}, \quad (21)$$

$$\blacktriangledown i_{L, off} = \frac{1}{L} \int_{t_{on}}^{t_{on}+t_{off}} V_L dt = \frac{V_{in} - V_{out}}{L} t_{off}. \quad (22)$$

Then, the stored energy in the inductor is given by $\blacktriangle i_{L, on} + \blacktriangledown i_{L, off} = 0$. Since a PWM drives the switching among states, the duty cycle is defined in terms of the on-state time (t_{on}) and the switching period (T) as $D = t_{on}/T$, resulting in a model for the step-up DC-DC boost converter such that [22]:

$$D = 1 - \frac{V_{in}}{V_{out}}. \quad (23)$$

4 | FINITE ELEMENT MODELLING

In this section, the electromagnetic performance of the FEM-designed inductor by the holistic approach in Figure 2, whose parameters are listed in Table 2, is assessed. To this end, the inductor is implemented in JMAG[®] software.

Following the holistic design, the geometry, operational conditions, meshing quality, materials' properties and their characteristics, are established previously.

TABLE 2 JMAG simulation parameters.

System ratings	
Rated power, ripple current	300 W, 1 A
Input current source (I_m)	4.7 A
Simulation sample time	5 μ s
Number of steps	1000
Simulation time	5 ms
Inductor parameters	
Core saturation flux	1.6 T
Permeability of the core	40 μ_0
Inductance factor, leakage inductance	275 nH/T ² , 50 μ H
Coil resistance, inductance (L)	0.4 Ω , 1.77 mH
Switching frequency	18.31 kHz

TABLE 3 Dimensions of the inductor core.

Dimensions in millimeters					
A	B	C	D	E	F
80.01	48.10	29.72	28.04	18.20	19.80
G	H	I	L	M	—
2.00	28.00	4.50	9.91	19.80	—

TABLE 4 Materials and their characteristics.

Element	Core	Coil	Spool	Enclosure
Material type	00X8024E040	Copper	Plastic	Stainless steel
Characteristics				
Conductivity (S/m)	0.166667	5.8001 $\times 10^7$	1 $\times 10^{-21}$	1.45 $\times 10^6$
Density (Kg/m ³)	7850	8960	1000	7500

4.1 | Geometry

This consists of a 3D design that is implemented in SolidWork[®], according to dimensions summarized in Table 3 and rendering in Figure 5. It is integrated by three independent pieces such as a magnetic core, spool and coil. A three-column magnetic core is formed by two similar pieces creating an air gap among them; the plastic spool is used as an isolator; and a copper coil.

4.2 | Materials

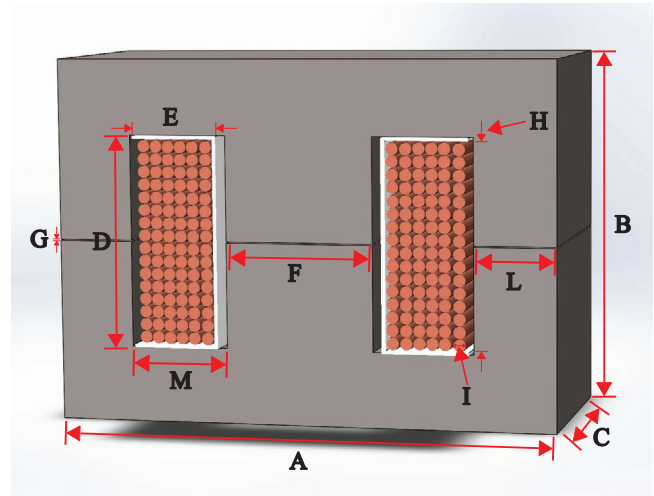
Table 4 summarizes the main materials and their characteristics. In this work, all electromagnetic materials are considered isotropic.

4.3 | Operational conditions

The magnetic flux density of the FEM-designed inductor is exhibited in Figure 6, reaching a peak of 0.86 Teslas. The induc-



(a)



(b)

FIGURE 5 Inductor Geometry. (a) Lateral view. (b) Measurements.

tor behavior under constant current conditions is displayed in Figure 8, where plot (a) shows an average inductance of 1.7 mH, plots (b) and (c) present voltage and current waveforms at 18.3 kHz, and plot (d) shows the instantaneous power.

4.4 | Mesh

The inductor model is discretized in Figure 6, resulting in 80596 elements and 40685 nodes. The discretization was accomplished by using equilateral triangles as elements to cover the surface model. Then, Maxwell's equations are solved by a homogeneous interpolation method that ensures the same potential at each node. If the triangles are not equilateral, then the interpolation is not feasible and increases the simulation time. The best quality of the mesh is defined as 1; meanwhile, a line is associated with the worst quality taking the value of zero, thus there is no interpolation surface. The mesh quality is displayed in Table 5. Notice that more than 94.5% of elements are between 0.7 and 1.0, which is considered a very good mesh quality [23], and about a 5.5% is between 0.2 and 0.7.

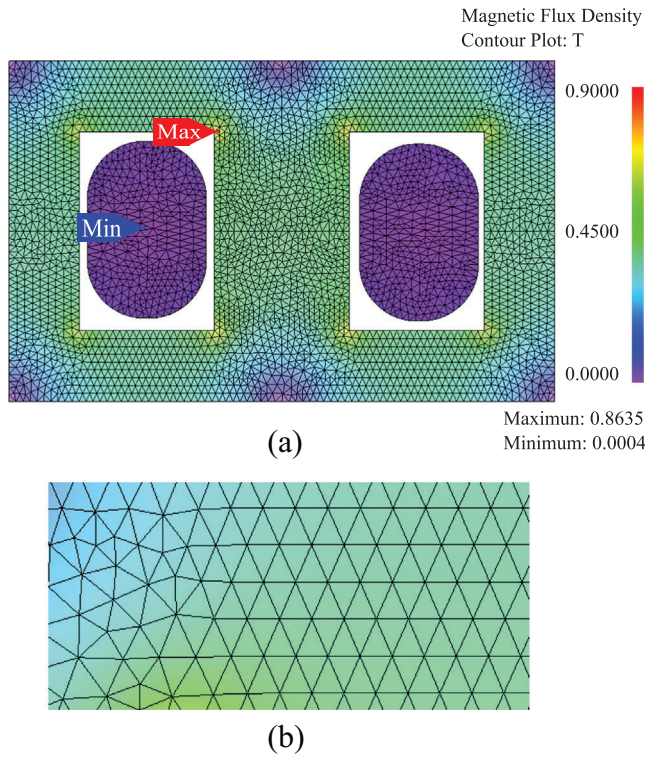


FIGURE 6 Inductor design via finite element method in JMAG. (a) Magnetic flux density operating at about 400 W. (b) Meshing for the inductor: 80,596 elements and 40,685 nodes.

TABLE 5 Quality of the mesh.

Quality	0.0–0.1	0.1–0.2	0.2–0.3	0.3–0.4	0.4–0.5
Element count	0	0	0	8	237
Quality	0.5–0.6	0.6–0.7	0.7–0.8	0.8–0.9	0.9–1.0
Element count	840	3304	11383	13833	50991

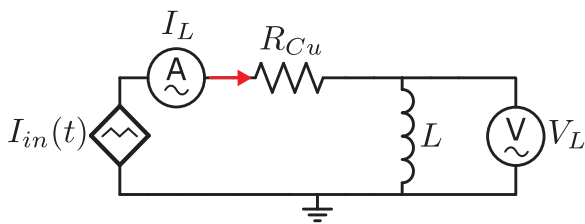


FIGURE 7 Circuit diagram in JMAG.

5 | SIMULATION, PROTOTYPE AND EXPERIMENTAL RESULTS

Once all target definitions are met and the FEM analysis is performed, the designed inductor is simulated in JMAG by supplying a current with a triangular waveform in (24), as depicted in Figure 7, similar to the current condition that is experienced in an actual DC-DC converter, resulting in the behaviors displayed in Figure 8a–d, where the waveforms for the power, voltage, current, and inductance are exhibited. Figure 8a show-

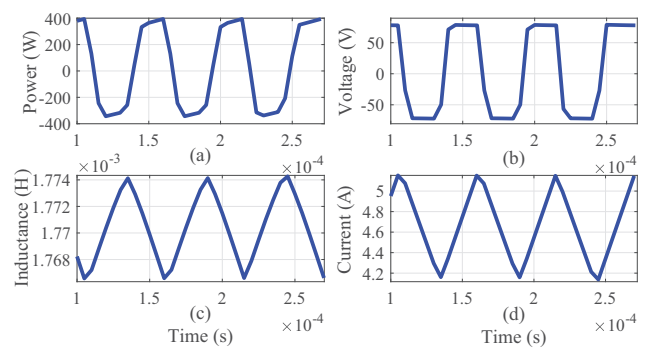


FIGURE 8 Behavior of the inductor when a current ripple is applied.

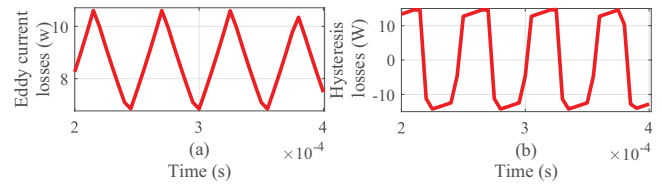


FIGURE 9 Core losses associated with Eddy currents and hysteresis at the input voltage (V_{in}) of 60 V.

cases the maximum power that was defined as target definitions at 300 W. From Figure 8b, it is possible to compute the RMS voltage, whose value is 69.98 V, differing 5.2% of the inductor voltage. An average inductance value of 1.77 mH is shown in Figure 8c. It is observed in Figure 8d that the triangular current has a DC offset of about 4.6 A, reaching a maximum current (i_{max}) at 5.2 A, and yielding constant changes in the voltage across the inductor that represent its charging and discharging process. Notably, all target definitions are met by following the holistic strategy in terms of maximum power, maximum current, and inductance. This fact is corroborated experimentally, as shown in the current I_L in Figure 12. This simulation was conducted according to the parameters in Table 2; likewise, all materials and their characteristics in Table 4 were added. The simulation required the following two conditions:

- FEM coil: This condition allows to establish that a current flows through the conductor linking it with the electric circuit.
- Symmetry boundary: This specifies the symmetry bound when the flow is perpendicular to one defined side, and it is used for all analysis types of electric fields.

$$I_{in}(t) = 4.2 \left(1 - \frac{2}{54.6 \times 10^{-6}} |t - \frac{54.6 \times 10^{-6}}{2} \left\lfloor \frac{t}{54.6 \times 10^{-6}} + \frac{1}{2} \right\rfloor \right) \quad (24)$$

To compute the core losses associated with Eddy currents and hysteresis losses according to (10) [16], the inductor is tested under voltage variations. These losses are shown in Figure 9, where can be observed the waveforms for both of them using

TABLE 6 Core losses associated with Eddy currents and hysteresis.

V_{in} (V)	L (mH)	Eddy current losses (W)	Hysteresis losses (W)
5	1.79	0.039	0.85
12	1.79	0.276	5.38
24	1.79	1.18	5.9
48	1.78	4.9	6.62
60	1.77	8.6	12.9

TABLE 7 Simulink simulation parameters.

System ratings	
Rated power, ripple current	300 W, 1 A
Voltage out (V_{out})	118
Voltage source (V_{in})	62.6 V
Simulation time	5 s
Snubber resistance	12 Ω
Snubber capacitance	220 pF
Capacitor (C)	500 μ F
Duty cycle (D)	0.5
Load resistor (R)	50 Ω
Coil resistance, inductance (L)	0.4 Ω , 1.77 mH
Switching frequency	18.31 kHz

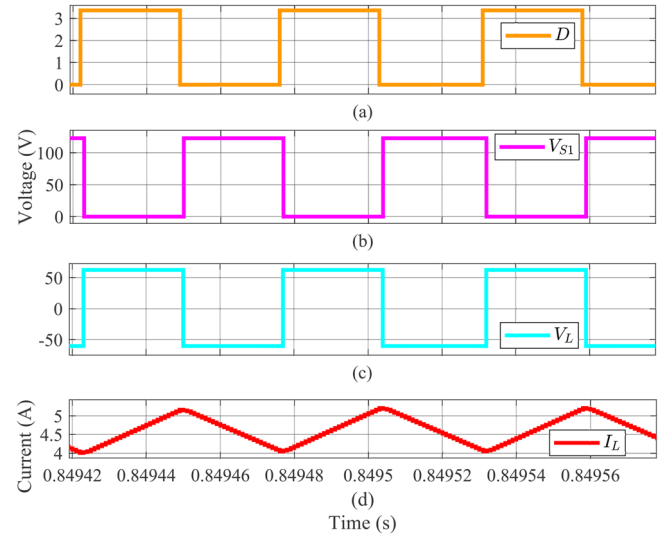
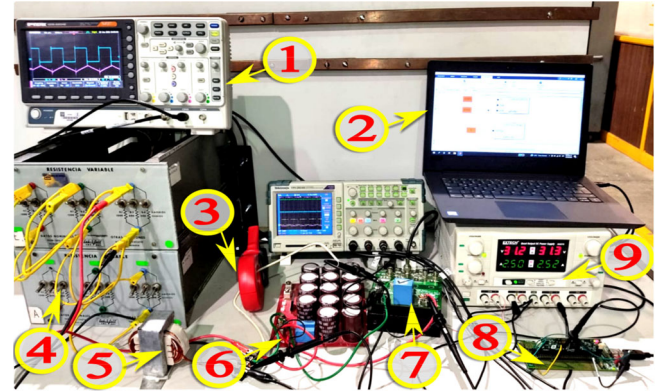
TABLE 8 Experimental parameters.

Parameter	Value
Inductor (L)	1.84 mH
Capacitor (C)	500 μ F
Load resistor (R)	50 Ω
MOSFET (S_1), diode (D)	C2M0080120D, MLBX1302T
Digital signal controller (DSC)	TMS320F28335
Switching frequency	18.31 kHz
Input Voltage Source (V_{in})	62.6 V

an input voltage (V_{in}) of 60 V. To verify the behavior of the inductor working at different operating points, the input voltage (V_{in}) is varied within the range between 5 V up to 60 V, as depicted in Table 6. Note that the core losses are proportional to the voltage rise.

As a second verification, the Simulink environment is used to replicate the behavior of the power converter circuit in Figure 1 by employing the parameters depicted in Table 7, such as resistance and snubber capacitance that are taken from the power device's datasheet [24]; likewise, the components' values reported in Table 8 are used. Notice the similitude between the simulated and actual responses that can also be corroborated through the waveforms for V_L and I_L in Figure 12 and for V_{S_1} in Figure 14.

Before proceeding with the experimental prototype, the step-up DC-DC boost converter in Figure 1 is implemented in the

**FIGURE 10** Simulation results in Simulink for D , V_{S_1} , V_L , and I_L .**FIGURE 11** Experimental testbed for the boost step-up DC-DC converter. (1) Scope, (2) PWM generator with Simulink, (3) AC/DC clamp, (4) resistive load, (5) inductor, (6) capacitor (C), (7) MOSFET power switch and diode (S_1), (8) DSC TMS320F28335, and (9) DC voltage source (V_{in}).

Matlab-Simulink environment with the parameters in Table 8. Once the converter is simulated, voltage and current responses in Figure 10 are obtained, where the orange waveform in plot (a) represents the PWM signal, the magenta waveform in plot (b) is the voltage over the power switch (S_1), the cyan waveform in the plot (c) indicates the voltage at the coil terminals, and the red waveform in the plot (d) showcases the current ripple that flows through the coil.

The design methodology's theoretical consistency and practical feasibility for inductors applied to power electronic circuits are experimentally verified with a laboratory testbed, as shown in Figure 11. Before the test, the inductance was measured with the UT-603 meter [25], resulting in a relative error of 4% compared to the calculated value. The test circuit and its modes of operation are addressed in Figure 1 and Section 3, respectively. The components used in the implementation of the prototype are summarized in Table 8, the implemented inductor is indicated with the number 5 in Figure 11.

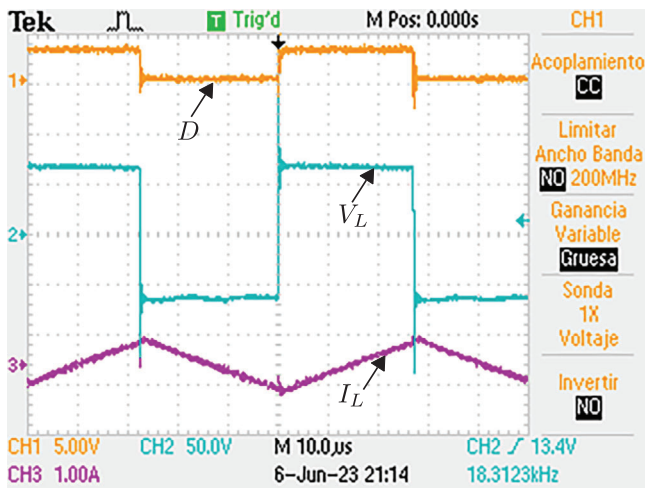


FIGURE 12 Experimental evaluation of D , V_L , and I_L under static conditions applied to the DC-DC boost converter.

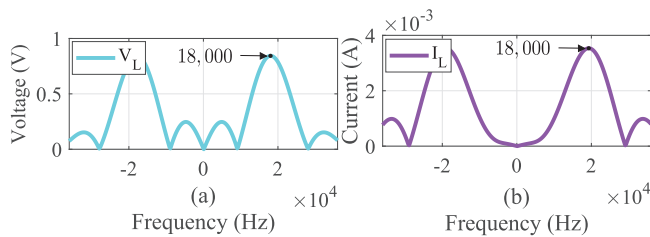


FIGURE 13 Fourier spectra of voltage and current waveforms at the inductor. (a) Inductor voltage (V_L). (b) Inductor current (I_L).

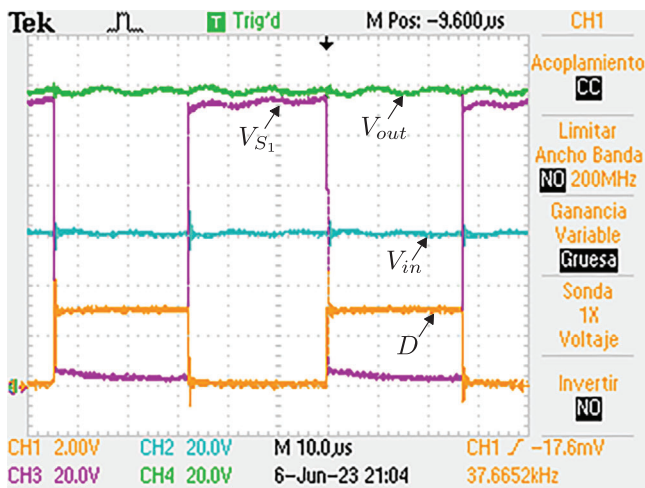


FIGURE 14 Experimental evaluation of D , V_{S1} , V_{in} and V_{out} under static conditions applied to the DC-DC boost converter.

Figure 12 shows the measurements of the PWM signal (orange line), the inductor voltage (L) (cyan line), and the current through the inductor (I_L) (violet line). When the switch is turned on, L stores energy in the form of a magnetic field, ramping its current according to (21). Under these conditions, the induced voltage rises up to 120 V, showing high-frequency oscillations in the turn-on and turn-off of the switch caused by parasitic reactances inside the MOSFET, the wires, and the cir-

TABLE 9 Comparisons between theoretical, simulated, and experimental results.

Method	Inductance (mH)
Proposed	1.77
Simulated in JMAG	1.77
Experimental	1.84

cuit paths. When the switch is off, the current of L decreases in a ramped pattern according to (22). The measured inductor current ripple is 1 A. This ripple is consistent with the theoretical calculations and those found in the magnetic simulation with JMAG software. Notice that Fourier spectra of voltage and current waveforms at the inductor in Figure 13 reflect symmetrical spectra and the fundamental frequency at 18 kHz, consistent with the commutation frequency.

Figure 14 details the measurements performed on the circuit for V_{in} , V_{out} , V_{S1} and D under stationary conditions. The figure shows how the circuit effectively raises the voltage at its output to 120 V (green line) with its respective input voltage (blue line), set at 60 V. When S1 is on, the capacitor at the output supplies power to the load, enabling the load voltage to be regulated.

6 | DISCUSSION

Following the proposed strategy in Figure 2, the theoretical value for the inductance that complies with all target definitions is 1.77 mH, as summarized in Table 9, which is also verified via JMAG simulation as reported in Figure 8c. The last validation was the experimental one, where the inductance value reached a value of 1.84 mH, attaining a 4% relative error in comparison with the theoretical and simulated values.

An alternative to measure the effectiveness of the current design methodology is to compare our results with other recent related work. For example, in [26], a characterization of variable inductors by finite element analysis (FEA) reports a mean squared error of 1.6% between FEM simulations and experimental results. However, based on the graphical results of [26], the error is not uniform along the load current level. The smaller the current, the bigger the error. On the other hand, [27] shows the design and model of filter inductors. The inductor constructive reaches 75–77% of the required inductance. In [28], the inductance leakage in a transformer design for a power converter was estimated with an error of less than 20%. Our methodology has a marginal error below 4% between the design's analytical, simulated, and experimental values.

7 | CONCLUSIONS

This paper has demonstrated a straightforward and accurate methodology to design and implement an inductor for

properly making part of a step-up DC-DC boost power electronic converter. The key idea behind this methodology lies in conveying the preliminary analytical design that is validated via simulations using the FEM and power electronic converters supported by JMAG and Matlab & Simulink, respectively. Also, this methodology is validated by implementing an experimental prototype of a step-up DC-DC boost converter and quantifying the inductor response, achieving all target specifications, such as maintaining a current ripple of approximately 1 A.

AUTHOR CONTRIBUTIONS

Elean Jim Martínez-Salgado: Conceptualization; data curation; formal analysis; investigation; methodology; software; validation; visualization; writing—original draft. **Gabriel E. Mejía-Ruiz:** Conceptualization; formal analysis; investigation; methodology; supervision; writing—original draft. **José Manuel Ramos-Guerrero:** Data curation; investigation; methodology; software; writing—original draft. **Mario R. Arrieta Paternina:** Conceptualization; formal analysis; investigation; methodology; project administration; supervision; validation; visualization; writing—original draft; writing—review and editing. **Javier de la Cruz:** Conceptualization; formal analysis; investigation; methodology; software; supervision. **Harold R. Chamorro:** Funding acquisition; resources; writing—review and editing.

ACKNOWLEDGEMENTS

The authors gratefully acknowledge financial support from the Project Support Program for Research and Technological Innovation of UNAM (DGAPA, PAPIIT-2023-2025) through the project IT102723.

CONFLICT OF INTEREST STATEMENT

The authors declare no conflicts of interest.

DATA AVAILABILITY STATEMENT

Data available on request from the authors: The data that support the findings of this study are available from the corresponding author upon reasonable request.

ORCID

Mario R. Arrieta Paternina  <https://orcid.org/0000-0002-2121-6420>

Harold R. Chamorro  <https://orcid.org/0000-0003-2128-2425>

REFERENCES

- Forouzesh, M., Siwakoti, Y.P., Gorji, S.A., Blaabjerg, F., Lehman, B.: Step-up dc-dc converters: A comprehensive review of voltage-boosting techniques, topologies, and applications. *IEEE Trans. Power Electron.* 32(12), 9143–9178 (2017)
- Gopal, Y., Birla, D., Lalwani, M.: Reduced switches multilevel inverter integration with boost converters in photovoltaic system. *SN Appl. Sci.* 2(1), 58 (2019). <https://doi.org/10.1007/s42452-019-1848-7>
- Rodríguez, J.R., Mejía Ruiz, G.E., Paternina, M.R.A., Velázquez Ibanez, A., Salgado Herrera, N.M., Santoyo Anaya, M.A., et al.: A single-loop and current-sensorless control for on-grid seven-level photovoltaic microinverter. *IET Power Electron.* 16(6), 905–916 (2023). <https://ietresearch.onlinelibrary.wiley.com/doi/abs/10.1049/pel2.12436>
- Axelrod, B., Berkovich, Y., Ioinovici, A.: Switched-capacitor/switched-inductor structures for getting transformerless hybrid dc-dc pwm converters. *IEEE Trans. Circuits Syst. I Regul. Pap.* 55(2), 687–696 (2008)
- Huang, Y.Y., Lai, Y.S.: Optimal inductor design method for gan-based pfc. *IEEE Access* 11, 104452–104462 (2023)
- McLyman, C.W.T.: *Transformer and Inductor Design Handbook*. CRC Press, Boca Raton, FL (2019)
- Kazimierczuk, M.K.: *High-Frequency Magnetic Components*. John Wiley & Sons, Chichester (2009)
- Kunstbergs, N., Hinz, H., Roll, D., Schofield, N.: Improved single-layer powder core inductor design procedure for dc-dc converters. *IET Power Electron.* 17(4), 494–510 (2024). <https://ietresearch.onlinelibrary.wiley.com/doi/abs/10.1049/pel2.12659>
- Sekiya, H., Kazimierczuk, M.K.: Design of rf-choke inductors using core geometry coefficient. In: *Proceedings of Electrical Manufacturing and Coil Winding Conference*. IEEE, Piscataway (2009)
- Saini, D.K., Ayachit, A., Reatti, A., Kazimierczuk, M.K.: Analysis and design of choke inductors for switched-mode power inverters. *IEEE Trans. Ind. Electron.* 65(3), 2234–2244 (2018)
- Gao, Y., Sankaranarayanan, V., Dede, E.M., Zhou, Y., Zhou, F., Erickson, R.W., et al.: Modeling and design of high-power, high-current-ripple planar inductors. *IEEE Trans. Power Electron.* 37(5), 5816–5832 (2022)
- Ayachit, A., Kazimierczuk, M.K.: Sensitivity of effective relative permeability for gapped magnetic cores with fringing effect. *IET Circuits Devices Syst.* 11(3), 209–215 (2017). <https://ietresearch.onlinelibrary.wiley.com/doi/abs/10.1049/iet-cds.2016.0410>
- Liao, H., Chen, J.F.: Design process of high-frequency inductor with multiple air-gaps in the dimensional limitation. *J. Eng.* 2022(1), 16–33 (2022). <https://ietresearch.onlinelibrary.wiley.com/doi/abs/10.1049/tje.2.12087>
- Guillod, T., Papamanolis, P., Kolar, J.W.: Artificial neural network (ann) based fast and accurate inductor modeling and design. *IEEE Open J. Power Electron.* 1, 284–299 (2020)
- Zhang, Z., Ngo, K.D.T., Nilles, J.L.: Design of inductors with significant ac flux. *IEEE Trans. Power Electron.* 32(1), 529–539 (2017)
- Jsol Corporation. JMAG version 18.1 user's manual: Iron loss formulas (2019)
- Kaltenbacher, M.: *Numerical Simulation of Mechatronic Sensors and Actuators*, vol. 2. Springer, Berlin (2007)
- Forouzesh, M., Siwakoti, Y.P., Gorji, S.A., Blaabjerg, F., Lehman, B.: Step-up dc-dc converters: A comprehensive review of voltage-boosting techniques, topologies, and applications. *IEEE Trans. Power Electron.* 32(12), 9143–9178 (2017)
- Liu, H., Hu, H., Wu, H., Xing, Y., Batarseh, I.: Overview of high-step-up coupled-inductor boost converters. *IEEE J. Emerg. Sel. Topics Power Electron.* 4(2), 689–704 (2016)
- Mejía-Ruiz, G.E., Paternina, M.R.A., Serna, J.A.d.l.O., Zamora-Mendez, A.: O splines-based fixed-frequency integral sliding-mode controller for pfc rectifier. *IEEE Trans. Power Electron.* 38(8), 9448–9458 (2023)
- Suárez-Velázquez, G.G., Mejía-Ruiz, G.E., García-Vite, P.M.: Control and grid connection of fuel cell power system. In: *2020 IEEE International Autumn Meeting on Power, Electronics, and Computing (ROPEC)*, vol. 4, pp. 1–5. IEEE, Piscataway (2020)
- Luo, F.L., Ye, H.: *Essential dc/dc converters* (2005). <https://api.semanticscholar.org/CorpusID:64423163>
- Fatchurrohman, N., Chia, S.: Performance of hybrid nano-micro reinforced mg metal matrix composites brake calliper: Simulation approach. In: *IOP Conference Series: Materials Science and Engineering*, vol. 257, p. 012060. IOP Publishing, Bristol (2017)
- Cree Power: KIT8020CRD8FF1217P-1 user manual (2024). https://media.digikey.com/pdf/data%20sheets/cree%20power/kit8020crd8ff1217p-1_um.pdf

25. Uni-Trend Technology: UT602/603 operating manual (2018). <https://meters.uni-trend.com/download/ut602-ut603-user-manual/>
26. Beraki, M., Trovao, J.P., Perdigao, M.: Characterization of variable inductors using finite element analysis. *Simul. Modell. Pract. Theory* 97, 101952 (2019)
27. Quinn, R.: Design and modelling of filter inductors for DC/AC converters. Master of Science Thesis, Tampere University (2022)
28. Sharma, A., Kimball, J.W.: Hybrid model to evaluate the frequency-dependent leakage inductance of partially-filled transformers. *Power Electron. Devices Comp.* 5, 100038 (2023)

How to cite this article: Martínez-Salgado, E.J., Mejía-Ruiz, G.E., Ramos-Guerrero, J.M., Paternina, M.R.A., de la Cruz, J., Chamorro, H.R.: Accurate design, simulation and implementation of AC/DC inductors for power electronic converters. *IET Power Electron.* 1–11 (2024). <https://doi.org/10.1049/pe.2.12764>